

SURFACE MODELLING OF CRYSTALLINE NON-METALLIC INCLUSIONS

R. Dekkers ¹⁾, C.F. Woensdregt ²⁾, P. Wollants ¹⁾

¹⁾ Dept. Metallurgy and Materials Engineering, Katholieke Universiteit Leuven, Belgium

²⁾ Faculty of Earth Sciences, Utrecht University, The Netherlands

INTRODUCTION

Crystalline non-metallic inclusions in liquid steel show a variety of forms. Spherical, faceted, plate-like, dendritic and cluster-like inclusions have been reported by several authors [1,2]. The form of the inclusions is determined by their structure, growth conditions and presence of impurities. Spherical and dendritic inclusions are typical for growth far from equilibrium at high supersaturation. In case the crystal grows at almost equilibrium conditions, its bulk crystal structure becomes more important and facets appear on the surface due to the anisotropy of the crystalline phase.

In the present paper, the theoretical growth form of spinel (MgAl_2O_4) is derived for the ideal crystal structure of normal spinel by means of the Hartman-Perdok theory. After the search for F faces, the attachment energies and specific surface energies are calculated in an electrostatic point charge model. These energies are corrected for Born repulsion and van der Waals attraction. In addition, the partial covalency of the strong is taken into account bonds by adjusting the effective point charges. We are able to describe the most favourable surface topology at atomic scale for the interfaces during the growth. Further the model is used to derive the growth form and equilibrium form of corundum. Finally the computed theoretical forms are discussed in relation to the morphologies of inclusions observed in steel.

Spinel can be present as non-metallic inclusions in steel [3]. Hercynite (FeAl_2O_4) and galaxite (MnAl_2O_4) have been observed in semi-killed steels and are possibly the precursors of aluminium oxide. Spinel (MgAl_2O_4) can even be present in completely killed steel. Magnesiochromite (MgCr_2O_4) refractory bricks are used in steel industry as furnace lining, because they are very resistant to corrosion by slag [3,4]. The $\gamma\text{-Al}_2\text{O}_3$ phase, which has been observed in steel [5], crystallises in a spinel defect structure.

Corundum ($\alpha\text{-Al}_2\text{O}_3$) is energetically the most stable aluminium oxide structure. Cluster-type inclusions have been determined to be corundum [6]. This work shows that single faceted corundum particles in steel can be recognised as well.

THE HARTMAN-PERDOK THEORY

The Hartman-Perdok Theory (HPT) describes the relation between internal crystal structure and crystal morphology [7-9]. Moreover, it derives at the same time the surface topology of the crystalline interface during the growth at atomic scale.

1. Periodic Bond Chains

The PBC is an uninterrupted periodic chain of strong bonds between the crystallising units, such as ions, molecules, atoms or clusters thereof, formed during crystallisation. A PBC must be stoichiometric. At the same time, it should not have a dipole moment perpendicular to its direction $[uvw]$. Only a limited number of PBCs can be distinguished in a crystal structure, assuming that strong bonds are confined to the first co-ordination sphere. In a projection of the three-dimensional crystal structure parallel to the vector translation of the PBCs (figure 1a) they are seen end-on as open circles. The detachment of growth units parallel to the PBCs is easier for C than for A , when additional strong bonds are present between A and B . These latter bonds form another PBC parallel to the crystal surface. Hence the growth of such a flat or F face proceeds via a layer mechanism if two or more PBCs are parallel to its surface. In figure 1b strong bonds between A and B are absent, which results in a stepped or S face as the probability of detachment for A and C are equal.

2. Crystal faces

Crystal faces can be classified either as F faces, which contain at least two PBCs in a slice of thickness d_{hkl} , or as S faces containing only one PBC, or as K faces containing no PBC at all (figure 2). The F faces are the slowest to grow according to a layer mechanism and are therefore the only important ones for the crystal morphology. K faces grow quickly without nucleation. S faces are intermediate between F and K faces. Although they need a one-dimensional nucleation in case of low kink densities, in practice there are always sufficient kinks present. Just as K faces, they grow so fast that they should not be present on growth forms.

PBCs, F , S and K faces are structurally defined and cannot be determined experimentally. It is, however, possible to observe growth spirals or two-dimensionally nucleated layer growth indirectly ex-situ or directly in-situ by STM or AFM. Both phenomena are indications for an F character of that particular face.

For the quantification of the morphological importance, Hartman defines the attachment energy, the energy related to the surface of the elementary growth layer. The surface structure of a growing crystal is determined by its specific surface energy that must be as low as possible. The distances between two identical surfaces are equal to the interplanar spacing. When the unit cell is cantered and/or screw axes or glide planes are present perpendicular to that face (hkl), the repeat distance of the minimum in specific energy may be submultiples of d_{hkl} : d_{nhkn} . The extinction rules of X-ray crystallography will thus also be valid for the thickness of the elementary growth layer just as in case of the Bravais-Friedel-Donnay-Harker law. Hence the Hartman-Perdok theory considers the slice with a thickness of d_{hkl} as the elementary growth layer.

The identification of PBCs and subsequent classification of crystal faces as F , S and K faces can be of great value in understanding the crystal morphology. The slice with an F character defines, however, not only the elementary growth layer in case of layer growth, but also the topology of the crystalline interface during the crystal growth processes on atomic scale. Hence the influence

of the crystal structure on the surface configuration of the crystalline interface can be derived with atomic precision by the Hartman-Perdok method.

QUANTITATIVE APPROACH

1. Attachment energy

The attachment energy, E_{at} , is the energy released per mole, when a new slice of thickness d_{hkl} crystallises on an already existing crystal face (hkl). The attachment energy is, in fact, the sum of all the interaction energies between all the ions belonging to one crystallising unit and all the slices d_{hkl} into which the crystal has been divided parallel to the crystal face (hkl), see also figure 3. The slice energy, E_{sl} , is the energy released per mole, when a new slice d_{hkl} is formed from the vapour neglecting the influence of edge energies. The crystal energy, E_c , is the energy released per mole, when the crystal crystallises from the vapour. The following relation holds between the crystal energy, the attachment energy and the slice energy:

$$E_{cr} = E_{sl} + E_{at}. \quad (1)$$

2. Specific surface energy

The specific surface energy, g^{hkl} , of a crystal face (hkl) is the energy per unit area of surface needed to split an infinite crystal in two halves along the boundary of two adjoining slices having a thickness d_{hkl} . The energy to split a crystal parallel to a face (hkl) along the slice boundary equals:

$$\sum_i iE_i \quad (2)$$

The summation over i times E_i is due to splitting of the crystal in two halves parallel to the slice boundary of (hkl), e.g., the boundary between the slices with number $m=0$ and 1 in figure 4. The interaction energies of slice 0 with slices 1, 2, 3, etc. equals E_1, E_2, E_3 , etc. In case of slice 2 these energies are E_2, E_3 , etc., respectively. For the calculation of the specific surface energy the number of molecules within a slice per unit area of the surface must be known. Hence the specific surface energy can be calculated from the following expression

$$g = \frac{fZ_p d_{hkl}}{2V_p} \sum_{m=1}^{\infty} mE_m \quad (3)$$

where f (=166.036) is a conversion factor in order to obtain the surface energy in mJm^{-2} instead of kJ/mole , Z_p the number of molecules in the primitive unit cell with volume V_p and E_m the partial attachment energy of slice m .

3. The electrostatic point-charge model

In order to quantify the relative morphological importance of F faces obtained from the Hartman-Perdok analysis, attachment energies have been computed with the Fortran program ENERGY. Beside the attachment energies also slice energies and specific surface energies are calculated in an electrostatic point charge model.

The potential, V_p , at the point $P(R,Z)$ induced by an infinite row r of $2N$ equally spaced point-charges qe with spacing p can be calculated [7-12] as shown below. There are three different cases:

1. The point P is situated in a general position, where $R \neq 0$ and $Z \neq 0$ (figure 5a)

$$V_p(R,Z) = 2 \frac{qe}{p} \left[\sum_{l=1}^{\infty} p i H_o^{(1)} \left(2p \frac{lR}{p} \right) \cos \left(2p \frac{lZ}{p} \right) + \ln \left(\frac{2p}{R} \right) + \lim_{N \rightarrow \infty} N \right] \quad (4)$$

where the expression $iH_o^{(1)}(iy)$ represents the real part of the Hankel function of the zero order with an imaginary argument, of which the value decreases rapidly as the argument y increases [13].

2. The point P is situated on the row of point-charges, anywhere in between two point-charges, where $R = 0$ and $Z \neq 0$ (figure 5b)

$$V_p(0,Z) = -\frac{qe}{p} \left[\Psi \left(\frac{Z}{p} \right) + \Psi \left(1 - \frac{Z}{p} \right) - \left(\frac{p}{Z} \right) - \left(\frac{p}{p-Z} \right) \right] + 2 \frac{qe}{p} \lim_{N \rightarrow \infty} \ln N \quad (5)$$

where $\Psi(x) = \frac{d \ln x!}{dx}$

3. The point P is situated just at a site of a point-charge, $R=Z=0$ (figure 5c)

$$V_p(0,0) = 2 \frac{qe}{p} [C + \ln_{N \rightarrow \infty} N] \quad (6)$$

where: $C = -\Psi(0) = 0.57721566490$ (Euler's constant).

The actual version of the computer program (ENERGY99) computes now also the contributions of the Born repulsion energy and the attractive van der Waals energy to the surface and attachment energies. The point charges used in the models for spinel and corundum were taken from Matsui [14], who computed the ion net charges and coefficients for the short-range interactions from molecular dynamics simulations. These point charges and short-range interaction coefficients are listed in table 1. He approximates the potential energy by the sum of pair wise interactions, as in the following expression:

$$V(r_{ij}) = q_i q_j r_{ij}^{-1} - C_i C_j r_{ij}^{-6} + f(B_i + B_j) \exp[(A_i + A_j - r_{ij})/(B_i + B_j)] \quad (7)$$

where the terms represent Coulomb, dispersion and Born repulsion interactions, respectively. Here r_{ij} is the interatomic distance between atoms i and j , f is a standard force of $4.184 \text{ kJ } \text{\AA}^{-1} \text{ mol}^{-1}$, and q_i , A_i , B_i and C_i are the net charges, repulsive radii, softness parameters and van der Waals coefficients of the ion i , respectively. In his interatomic potential model the net charges are constrained by $q(\text{Mg}) = \frac{2}{3} q(\text{Al}) = -q(\text{O})$, in order to apply the potential to melts and crystals with any composition in the system $\text{CaO-MgO-Al}_2\text{O}_3\text{-SiO}_2$ (CMAS).

4. Theoretical growth form and equilibrium form

Hartman and Bennema [15] found that the relative growth rate of a face is directly related to attachment energy. Hence the theoretical growth shape of spinel can be constructed by means of a so-called Wulff plot construction. The distance from a central point to the face (hkl) is plotted directly proportional to the absolute value of the attachment energy of that face. The innermost closed surface of this three-dimensional plot represents the theoretical growth form. This theoretical growth form includes only the contributions to the relative growth rates from the ideal crystal structure. Other contributions, such as reconstruction or relaxation of the interface, the influence of supersaturation and the presence of impurities are not taken into account.

The theoretical equilibrium form is also constructed by means of the Wulff construction. Instead of the attachment energies, the specific surface energies are plotted.

APPLICATION TO SPINEL

1. The spinel structure

The spinel group compounds, which have the general chemical composition of AB_2O_4 , where $\text{A} = \text{Mg}^{2+}$, Fe^{2+} , Mn^{2+} , Zn^{2+} , etc., and $\text{B} = \text{Al}^{3+}$, Cr^{3+} , Fe^{3+} , etc. Spinel compounds crystallise in the cubic space group $\text{Fd}\bar{3}\text{m}$ (227) with 8 tetrahedral a sites and 16 octahedral d sites. The oxygens are located on the 32 e sites arranged in cubic-closed-packing layers. The cubic-closed-packing layers of anions alternate with cation layers. The unit cell contains eight molecules of AB_2O_4 . In the so-called normal spinel structure, all the divalent cations are located on the tetrahedral a sites, while all trivalent cations are exclusively on the octahedral d sites. In the inverse-spinel structure, half of the trivalent ions are on the tetrahedral a sites and the divalent cations occupy together with the other remaining half of the trivalent ion the octahedral d sites.

The spinel structure accommodates a large variety of cations [16,17]. The locations of the tetrahedral and octahedral sites are always the same and do not depend on the nature of the constituent cations. However, the general position of the anions, (u,u,u) , is depending on the relative size of the A and B cations. For the mineral spinel (MgAl_2O_4) used as model for the normal spinel compounds in the present paper $u = 0.361$ [18], which is close to the ideal close packing $u = 0.375$. The crystal structure data, fractional co-ordinates of the cations and anions [18] as used in the present paper are listed in table 2.

According to the Law of Bravais-Friedel-Donnay-Harker the larger the interplanar distance d_{hkl} , the more important face (hkl) is for the crystal morphology provided that the space group symmetry and the presence of symmetry operators such as glide planes and screw axes have been taken into account. For spinel the morphological importance should accordingly be: $\{111\}$, $\{220\}$, $\{113\}$, $\{400\}$ and $\{331\}$. Hence, the most important crystal form of spinel is the octahedron $\{111\}$ followed by the rhombic dodecahedron $\{110\}$.

2. F faces in spinel

The search for proto-PBCs (pPBCs) can precede the search for complete PBCs. These pPBCs are defined by a series of strong bonds providing the vector translation $[uvw]$ parallel to the periodicity of the PBC [19]. They are the backbones of the genuine PBCs, but they are most of the times neither stoichiometric nor non-polar. Due to the F centring of the cubic unit cell the shortest translations is $\langle \frac{1}{2} \frac{1}{2} 0 \rangle$. Parallel to $\langle \frac{1}{2} \frac{1}{2} 0 \rangle$ the following pPBC can be traced consisting of four strong bonds: Mg - O - Al - O - Mg. The latter Mg is identical to the first Mg by a translation of $\langle \frac{1}{2} \frac{1}{2} 0 \rangle$. In a projection of along $[1\ 1\ 0]$ (figure 6) the shaded areas within the slice boundaries represent the $[\frac{1}{2} \frac{1}{2} 0]$ pPBC.

Five F faces that are all parallel to $[\frac{1}{2} \frac{1}{2} 0]$ can be defined (figure 6). Within their corresponding slice boundaries, complete stoichiometric and non-polar PBCs can be defined. These F faces are in order of decreasing d_{hkl} : $d_{\bar{1}11}$ (4.662 Å), $d_{\bar{2}20}$ (2.855 Å), $d_{\bar{1}13}$ (2.435 Å), d_{004} (2.019 Å) and $d_{\bar{3}31}$ (1.853 Å). Besides these five F faces no other F faces can be defined for spinel.

Each of the F faces $d_{\bar{1}11}$, $d_{\bar{2}20}$ and d_{004} has two different F slices, called d_{hkl-t} and d_{hkl-o} , which respectively refers to the presence of complete $[\text{MgO}_4]$ tetrahedra or complete $[\text{AlO}_6]$ octahedra within the slice boundaries. In dotted lines an $[\text{AlO}_6]$ octahedron and a $[\text{MgO}_4]$ tetrahedron are denoted in slice $d_{\bar{1}11o}$ and slice $d_{\bar{1}11t}$, respectively (figure 6). Until the surface related energies are calculated, we do not decide which one of these two configurations might exist during the growth of spinel. Once these energies are known, the energetically most favourable surface topography may be selected.

3 Surface configurations

When ions are located exactly on the slice boundaries, they must be divided over two slices. This can often be realised in more than one way. In the so-called disordered boundary condition the ions are at random distributed over the two slices, i.e., each ion site is occupied for 50 %. This means that the occupancy of that particular site is 0.5, either in time or as the statistical average occupation of all sites on the surface. For the ordered configuration half of the sites is fully occupied (solid circles in figure 7) and the other half consists of vacancies (open circles in figure 7). Hence different surface configurations can be defined as function of the selected surface topology.

3.1 The $\{111\}$ surface configurations

Aluminium atoms are located on the boundaries of both types $d_{\bar{1}11}$ slices, but the number of aluminium atoms on the slice $d_{\bar{1}11r}$ boundary is three times that of slice $d_{\bar{1}11o}$. For $\{111\}_o$ only one ordered topology exists, but for $\{111\}_t$ there are two possibilities (figure 7), respectively denoted as $\{111\}_{t-c}$ (left) and $\{111\}_{t-d}$ (right).

3.2 The $\{220\}_o$ and $\{220\}_t$ surface configurations

Ordering of the surface configuration in both $\{220\}_o$ and $\{220\}_t$ affects only the aluminium sites. In $\{220\}_o$ the magnesium and oxygen atoms located at the surface are part of both the $[\frac{1}{2} \frac{1}{2} 0]$ PBC and the $[001]$ PBC. Therefore the only ordered surface configuration of $\{220\}_o$ consists of arrays of alternating occupied and unoccupied aluminium sites. The aluminium sites at the surface of $\{220\}_t$ are part of the $[\frac{1}{2} \frac{1}{2} 0]$ PBC and of the $[001]$ PBC. Only one surface configuration is possible, which consists of arrays of fully occupied and unoccupied aluminium sites.

3.3 The $\{113\}$ and $\{331\}$ surface configurations

The slice content of the F face $\{331\}$ can be defined within straight slice boundaries (d_{331}) or by assuming complete tetrahedra (d_{331r} , not shown). In the latter case the slice boundaries are not straight and pass between two edges of neighbouring tetrahedra. In both cases the aluminium sites at the boundaries are part of the $[\frac{1}{2} \frac{1}{2} 0]$ PBC. Therefore these aluminium sites cannot be halved and the ordered configuration is formed by alternating arrays of occupied and unoccupied sites along $[\frac{1}{2} \frac{1}{2} 0]$.

Like the slice d_{331r} the slice d_{113} contains complete tetrahedra, but since the aluminium sites at its boundaries sites are not part of the $[\frac{1}{2} \frac{1}{2} 0]$ PBC these sites can be halved or be ordered. Two ordered configurations are possible, first in arrays with alternating occupied and unoccupied sites along $[\frac{1}{2} \frac{1}{2} 0]$ and secondly alternating arrays of occupied and unoccupied sites along $[\frac{1}{2} \frac{1}{2} 0]$, respectively denoted in table 3 with $\{113\}_c$ and $\{113\}_d$.

4.5 The $\{400\}$ surface configurations

Since all atom sites in the slice d_{400r} are part of the pPBCs $[\frac{1}{2} \frac{1}{2} 0]$ and $[100]$ only one surface configuration is permitted. The surface contains two oxygen atoms and one aluminium atom per molecule of spinel. Except the magnesium atoms, all other atoms are located on the slice boundaries.

Another slice, d_{400} , with magnesium ions on the boundaries, can be constructed. The magnesium ions are distributed in an ordered manner. Magnesium ions and vacancies alternate with each other with a periodicity of $\langle 110 \rangle$.

4. Results

The net charges, repulsive radii, softness parameters and van der Waals coefficients as given by Matsui [13] and listed in table 1 have been used in order to compute the attachment energies, surface energies and crystal energies. Table 3 lists the attachment energies (E_{tot}) and specific surface energies (γ_{hkl}) of disordered and ordered surface configurations. The attachment energy has been divided in Coulomb interactions (E_C) Born repulsion (E_B) and van der Waals interactions (E_D). These energies are listed in order of decreasing d_{hkl} . The total crystallisation energy is equal to $-4602 \text{ kJ}\cdot\text{mol}^{-1}$, of which $-4733 \text{ kJ}\cdot\text{mol}^{-1}$ is due to the Coulomb interactions and $+131 \text{ kJ}\cdot\text{mol}^{-1}$ due to the short-range interactions.

The dispersion energy and the Born repulsion energy in the spinel structure are respectively -529 and $660 \text{ kJ}\cdot\text{mol}^{-1}$, which results in a net effect of less than three percent of the crystallisation energy. The Born repulsion decreases rapidly with increasing r , being the distance between the corresponding ions, in contrast to the dispersion energy contributions. Above the cut off value of 0.1 nm the contributions of Born energy and those of the dispersion energies are not significant for our calculations.

When we compare the disordered and ordered surface configurations, we observe that the ordered surfaces have always a lesser negative attachment energies than those with a disordered surface. In case of multiple slice configurations, the configurations with complete $[\text{MgO}_4]$ tetrahedra have lower negative attachment energies. This is especially significant for $\{111\}$ and $\{220\}$, where the alternative slice configurations, $\{111\}_o$ and $\{220\}_o$, contain complete $[\text{AlO}_6]$ octahedra. Hence ordering of the cations on the boundaries or the incorporation of complete Al octahedra instead of Mg tetrahedra results into lesser negative and thus more stable surfaces.

The theoretical growth form shows an octahedron $\{111\}$ and the equilibrium form shows a rhombic dodecahedron. The importance of the octahedral face is caused by the strong influence of the cubic-closed packing of oxygen atoms parallel to $\{111\}$. Based on our computations, we suggest that the surface structure of the octahedral face consists of an oxygen layer with magnesium and aluminium atoms as interstitials between oxygen atoms. Other forms than $\{111\}$ present on spinel must be due to external conditions during the growth such as supersaturation and the presence of impurities.

APPLICATION TO CORUNDUM

Corundum was one of the first structures analysed by Hartman in 1962 [20]. In 1980 the PBC analysis was reviewed and slightly adjusted. Eight F faces were recognised, which are in decreasing order of d_{hkl} : (111) , (100) , (011) , (121) , $(01\bar{1})$, (021) , (222) and (200) . The attachment energies of a model with complete ionic charges were computed by the use of an earlier version of the computer program ENERGY and the growth form was found to be rhombohedral (left crystal in figure 9) [21]. The deviation from the more platy $\{111\}$ habit was explained as a habit modification caused by specific adsorption of the flux material on $\{111\}$.

In the present paper we use the point charges given by Matsui and include the short-range interactions [13]. Only the most important F faces have been computed (table 4). In order of decreasing attachment energy the following F slices have been computed: (100), (011), (111), $(01\bar{1})$, (121) and (021).

The effects of the short-range interactions on the attachment energies differ largely. There is only a minor correction of $0.7 \text{ kJ}\cdot\text{mole}^{-1}$ in case of (011), while in case of (100) the correction is $209 \text{ kJ}\cdot\text{mole}^{-1}$. These short-range interactions have a strong impact on the Coulomb interactions, which are much lower for the model based on the Matsui net charges than for the previous completely ionic model. The theoretical growth form is significantly changed (middle crystal in figure 9). The previous rhombohedral habit $\{101\}$ is changed into a habit that is more flattened parallel to $\{111\}$ with $\{100\}$ as the major rhombohedron and $\{101\}$ as the minor rhombohedron. The more equidimensional theoretical equilibrium form shows again $\{101\}$ as major rhombohedron and additional smaller forms such as $\{111\}$, $\{121\}$, $\{100\}$ and $\{01\bar{1}\}$ (right crystal in figure 9).

OBSERVED CRYSTAL FORMS

Spinel-type crystals such as, spinel, galaxite, hercynite and impure magnesiumchromite, observed in steel are usually octahedral (figure 10a). Sometimes cube-octahedral forms of galaxite-hercynite inclusions (figure 10b) and magnesium containing aluminium oxide inclusions have been observed as well. The rhombic dodecahedron equilibrium form has not been observed.

Aluminium oxide crystals have been observed that are almost similar to the computed growth form of corundum (figure 10c). The small deviation from the theoretical form, an increased morphological importance of $\{111\}$, might be due to the relatively fast growth process. This hypothesis is supported by the presence of a concave hopper-like $\{111\}$. The theoretical equilibrium form of corundum is less frequently observed (figure 10d) due to the fact that growth at equilibrium is hardly achieved.

Acknowledgements

This research has been partially financed through an IWT project (02.0117).

REFERENCES

1. T.B. Braun, J.F. Elliott and M.C. Flemings, *Met. Trans. B*, 10B (1979) 171-184.
2. R. Dekkers, B. Blanpain, P. Wollants, F. Haers, C. Vercruyssen and L. Peeters, in *EPD Congress 1999*, Ed; B. Mishra (The Minerals, Metals & Materials Society, 1999) 269-277.
3. K. Goto, B.B. Argent and W.E. Lee, *J. Am. Ceram. Soc.*, 80 (1997) 2, 461.
4. R. Kiessling, in *Non-metallic inclusions in steel* (The Institute of Metals, London, 1978).
5. A. Adachi, N. Iwamoto and M. Ueda, *Trans. ISIJ*, 6 (1966) 24-30.

6. E. Steinmetz, H-U. Lindenberg, W. Mörsdorf and P. Hammerschmid, Stahl und Eisen, 97 (1977) 23, 1154-1159.
7. P. Hartman, in *Crystal Growth: an Introduction*, Ed. P. Hartman (North-Holland Publishing Cy, Amsterdam, 1973), Chap 14, 367-402.
8. P.Hartman, in *Morphology of Crystals*, Ed. I. Sunagawa (Terra Scientific, Tokyo and Reidel, Dordrecht, 1988) part A, Ch.4, 269
9. C.F. Woensdregt, Phys. Chem. Minerals 19 (1992) 52-58.
10. E. Madelung, Phys Zeitschr 19 (1918) 524–533.
11. W. Kleber, N. Jahrb Mineral Geol Palaeontol Bd A (1939) 72-81.
12. P. Hartman, Acta Crystallogr. 9 (1956) 569-572.
13. E. Jahnke, Emde F und Lösch F, Tafeln höherer Funktionen, Sechste Auflage.BG Teubner Verlagsgesellschaft Stuttgart (1960).
14. M. Matsui, Phys. Chem. Minerals 23 (1996) 345-353.
15. P. Hartman and P. Bennema, J. Crystal Growth 49 (1980) 145-156.
16. G.D. Price, S.L. Price and J.K. Burdett, Phys. Chem. Minerals 8 (1982) 69.
17. W.A. Deer, R.A. Howie and J. Zussman, in *An Introduction in the Rock-Forming Minerals*, 2nd ed., Longman Group UK Lim., 1992) 558.
18. P. Villars and L.D. Calvert, 2nd ed., Vol. 1, ASM International (1991) 906.
19. C.F. Woensdregt, H.W.M. Janssen, A. Gloubokov and A. Pajaczowska, J. Crystal Growth, 171, 392.
20. P. Hartman, Zap. Vses. Mineral Obshch. 91 (1962) 672-682.
21. P. Hartman, J. Crystal Growth 49 (1980) 166-170.

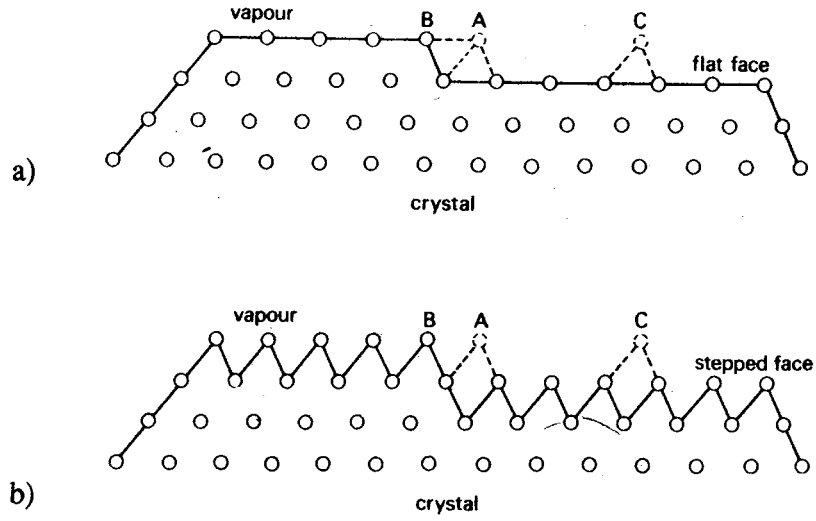


Figure 1: Three-dimensional crystal structure has been projected parallel to the direction of the PBC. PBCs are seen end-on as open circles a) *F* or Flat faces grow according to a layer mechanism, if they are parallel to at least two non-collinear PBCs b) Stepped or *S* faces are parallel to only one set of PBCs. Taken from [7].

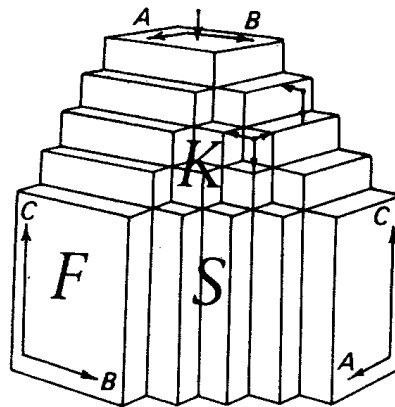


Figure 2: Classification of *F*-, *S*- and *K*-faces. Taken from [7].

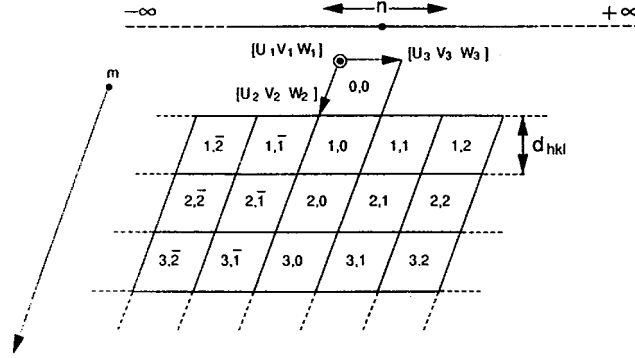


Figure 3: One crystallising unit is attached on an already existing crystal face (hkl) of a half crystal divided into m slices each d_{hkl} thick. Each crystallising unit contains a PBC (m,n), where m represents the slice number, and n the chain number. Taken from [9].

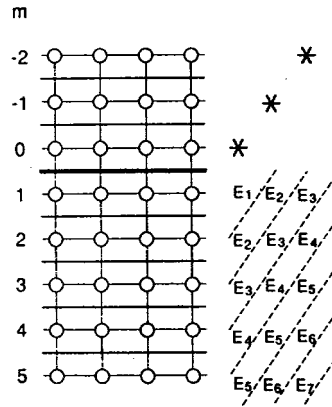


Figure 4: The energy needed to split the crystal along the slice boundary between the slices with slice number $m=0$ and 1 amounts to $\sum_i iE_i$.

Taken from [9].

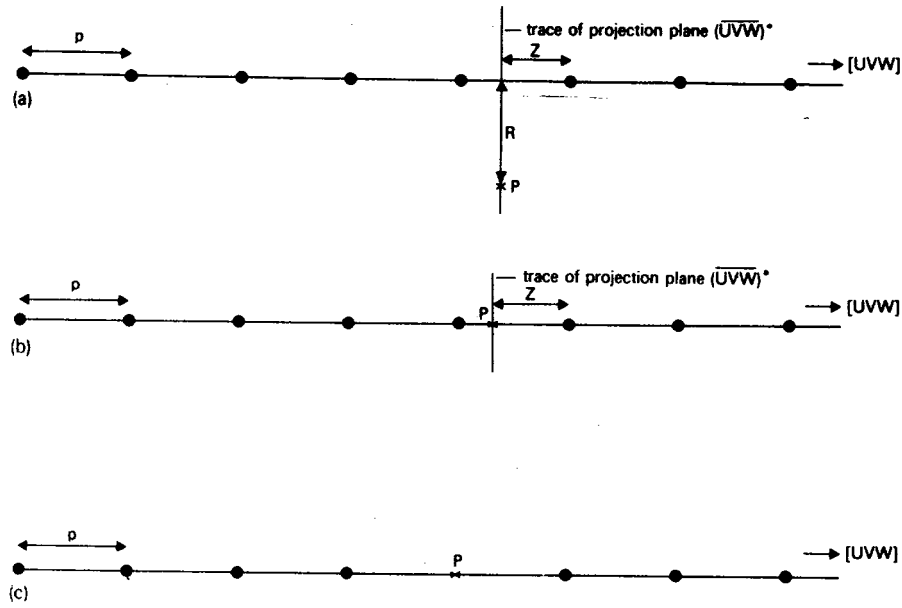


Figure 5: Position of point $P(R, Z)$ with respect to row of ions parallel to $[U_1 V_1 W_1]$ having a period p . The projection plane $(\overline{U_1 V_1 W_1})^*$ perpendicular to $[U_1 V_1 W_1]$ is chosen through $P(R, Z)$

- a) P in general position: $R \neq 0, Z \neq 0$
- b) P on the row of ions: $R = 0, Z \neq 0$
- c) P on an ion site: $R = Z = 0$.

Taken from [9].

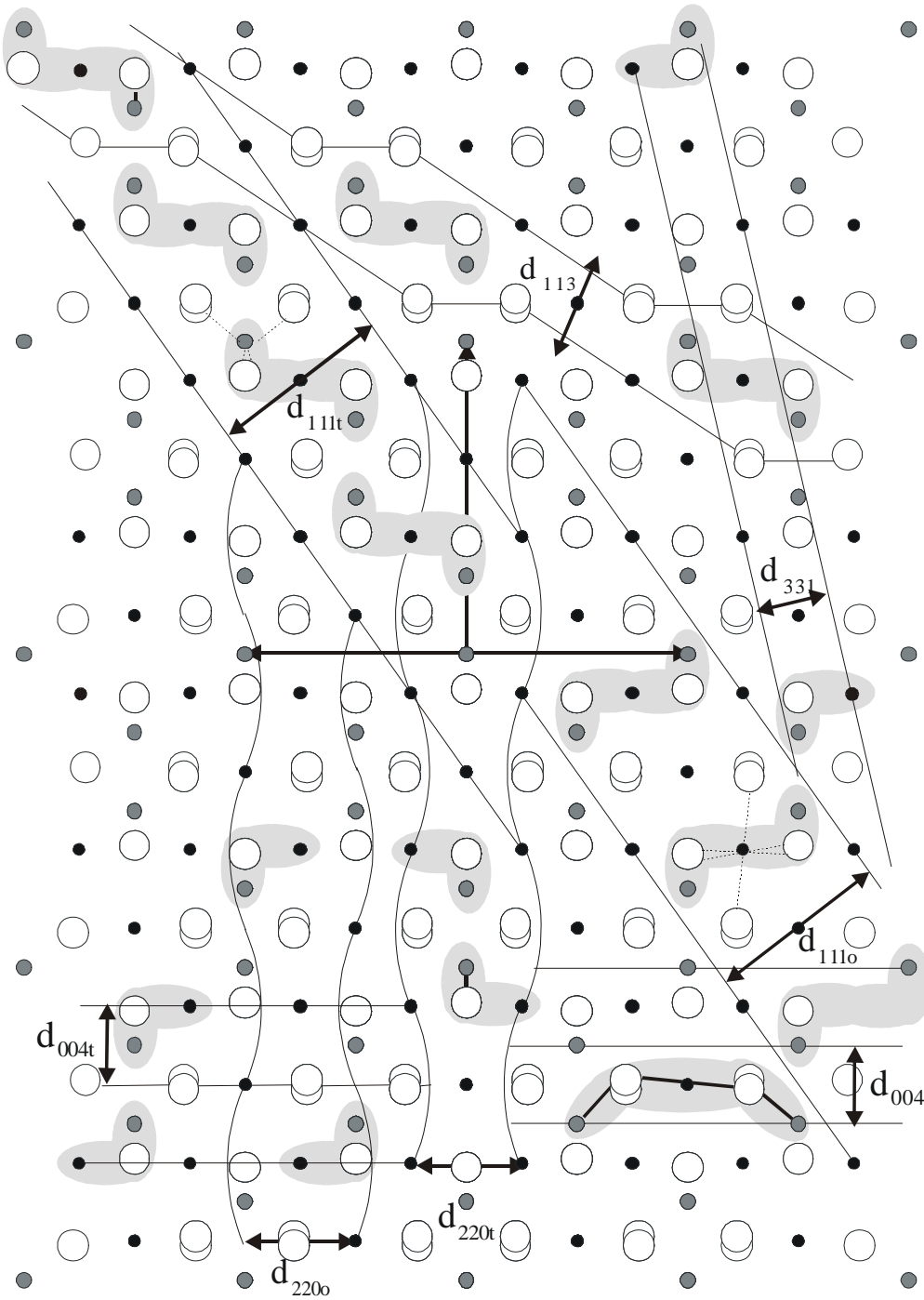


Figure 6: Projection of the spinel structure along $[\frac{1}{2} \frac{1}{2} 0]$. The grey areas, open circles, black circles and grey circles represent $\langle \frac{1}{2} \frac{1}{2} 0 \rangle$ pPBCs, oxygen atoms, aluminium atoms and magnesium atoms, respectively.

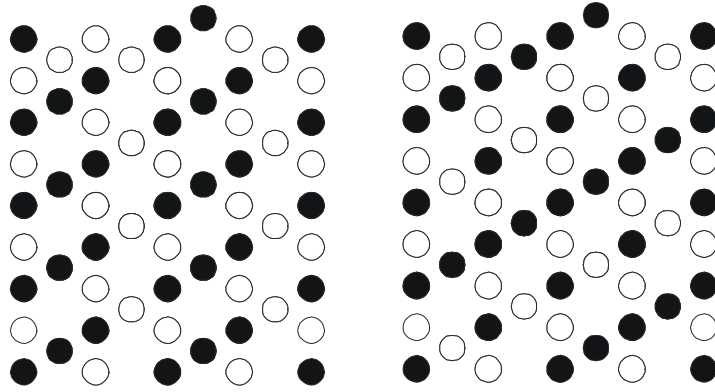


Figure 7: Two ordered surface configurations of $\{111\}_t$. Only the aluminium sites are shown. Solid circles and open circles respectively represent occupied aluminium sites and aluminium vacancies (left, $\{111\}_{t-c}$ and right, $\{111\}_{t-d}$).

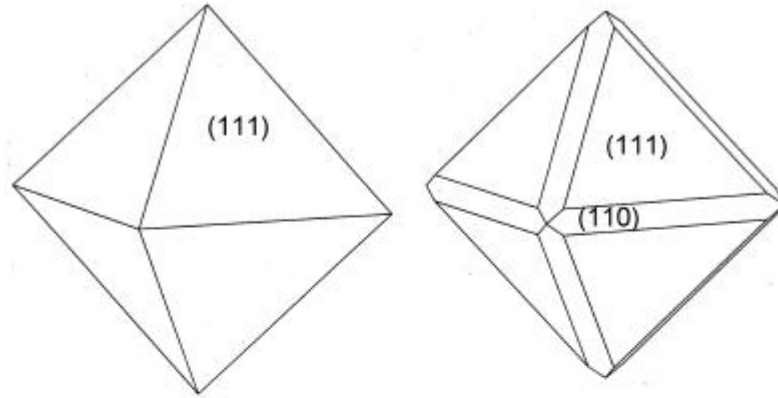


Figure 8: The theoretical growth form (left) and the theoretical equilibrium form (right) computed for spinel by using the data of Matsui [14]. The short-range contributions are included in the computation of the growth form.

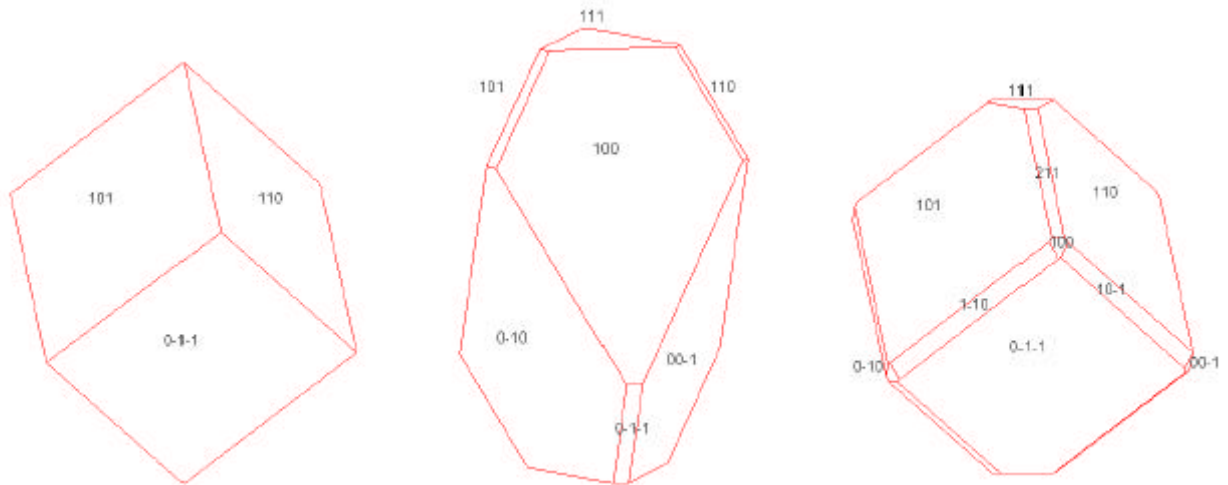


Figure 9: Theoretical corundum crystal forms. At the left the growth form as computed by reference [21] taking into account only the Coulomb long-range interactions. The growth form (middle) and equilibrium form (right) computed by using the data of Matsui [14]. The short-range contributions are included in the computation of the growth form.

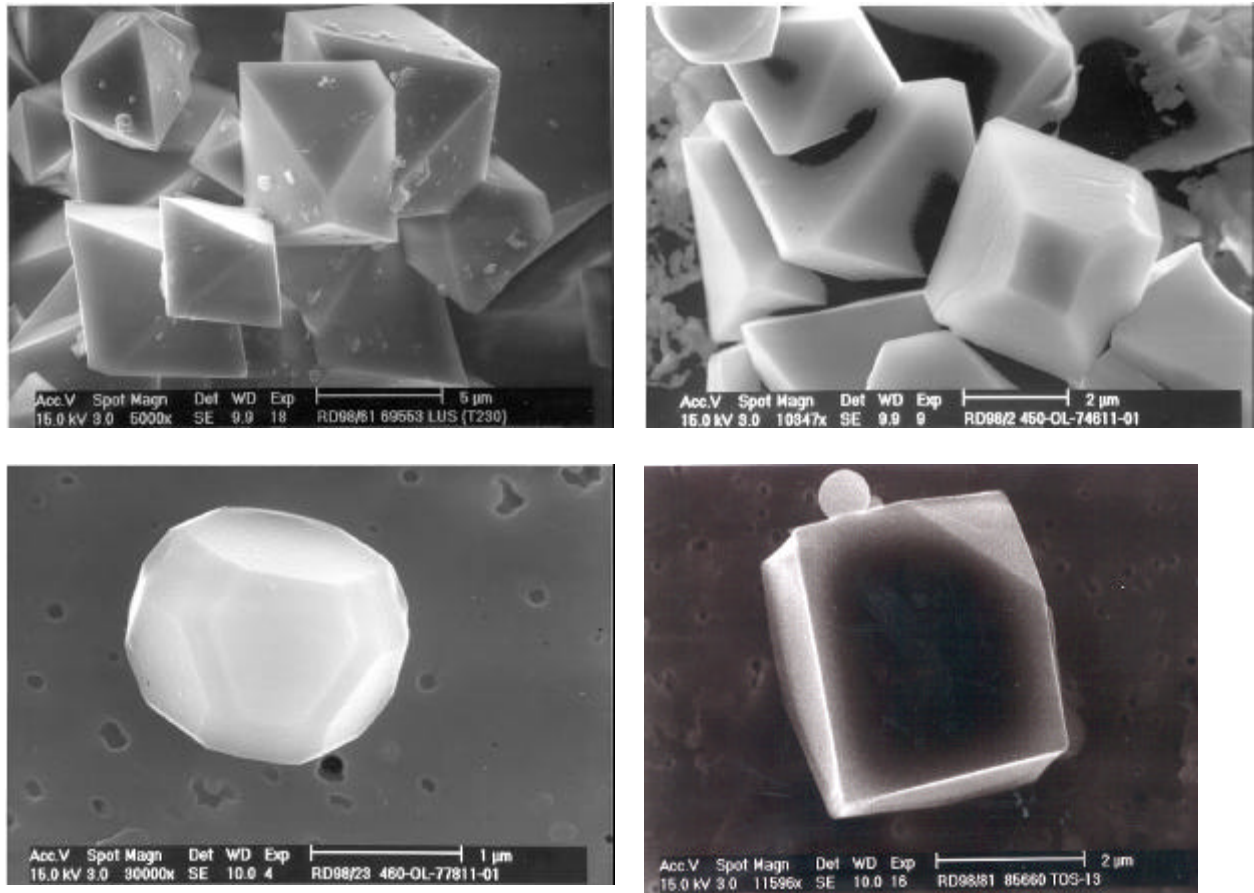


Figure 10: (a) Cluster of octahedral spinel crystals. (b) Hercynite-galaxite inclusions. (c) Growth form of corundum. (d) Equilibrium form of corundum.

Table 1: The net charges (q), repulsive radii (A), softness parameters (B) and van der Waals coefficients (C) are taken from Matsui [14].

| Atom | q [$ e $] | A [\AA] | B [\AA] | C [$\text{\AA}^3(\text{kJ/mol})^{1/2}$] |
|------|---------------|----------------------|----------------------|---------------------------------------------|
| O | 0.945 | 0.8940 | 0.040 | 29.05 |
| Al | 1.4175 | 0.7852 | 0.034 | 36.82 |
| Mg | -0.945 | 1.8215 | 0.138 | 90.61 |

Table 2: Crystal structure data of spinel (MgAl_2O_4) [17]. Unit cell data: Space group $\text{Fd}\bar{3}m$ (227), origin at ($\bar{4}3m$); $a_0 = 8.075 \text{ \AA}$.

| Atom | Wyckoff notation | point symmetry | x | y | z |
|------|------------------|----------------|-------|-------|-------|
| O | 32(e) | $3m$ | 0.361 | 0.361 | 0.361 |
| Al | 16(d) | $\bar{3}m$ | 5/8 | 5/8 | 5/8 |
| Mg | 8(a) | $\bar{4}3m$ | 0 | 0 | 0 |

Table 3. Computed energies (in kJ.mol⁻¹) for spinel with disordered (D) and ordered (O) surface configurations (γ_{hkl} in mJ.m⁻²). The attachment energies (E_{at}) and slice energies (E_{sl}) are divided in Coulomb (E_C), dispersion (E_D) and Born repulsion (E_B) energies. The subscript is explained in the text.

| Slice d_{hkl} | | E_{at} | | | | γ_{hkl} |
|----------------------|---|-------------------|------------------|--------------------|-----------|----------------|
| | | E_D | E_B | E_C | E_{tot} | |
| {111} _o | D | -200 | 253 | -346 | -288 | 509 |
| {111} _o | O | -200 | 253 | -265 | -209 | 762 |
| {111} _t | D | -124 | 79 | -1163 | -1196 | 1711 |
| {111} _{t-c} | O | -124 | 79 | -745 | -783 | 4380 |
| {111} _{t-d} | O | -124 | 79 | -744 | -783 | 4376 |
| {220} _o | D | -273 | 311 | -985 | -947 | 1720 |
| {220} _o | O | -273 | 332 | -651 | -605 | 870 |
| {220} _t | O | -209 [*] | 151 [*] | -1374 [*] | -1193 | ND |
| {113} | D | -261 | 210 | -1267 | -1567 | 3981 |
| {113} _c | O | -261 | 210 | -1272 | -1323 | 3921 |
| {113} _d | O | -261 | 210 | -1191 | -1230 | 3731 |
| {400} | O | -363 [*] | 439 [*] | -661 [*] | -584 | 1683 |
| {400} _t | O | -310 [*] | 264 [*] | -832 [*] | -878 | ND |
| {331} _t | O | -318 | 269 | -1309 | -1358 | 4054 |
| {331} | O | -347 | 383 | -1416 | -1349 | 2979 |

^{*} Calculated by $E_{at} = E_{cr} - E_{sl}$. ND, not determined.

Table 4. Computed energies (in kJ.mol^{-1}) for corundum. All faces concern ordered (O) surface configurations (γ_{hkl} in mJ.m^{-2}). The attachment energies (E_{at}) and slice energies (E_{sl}) are divided in Coulomb (E_{C}), dispersion (E_{D}) and Born repulsion (E_{B}) energies.

| Slice d_{hkl} | | E_{at} | | | | γ_{hkl} |
|-----------------|---|-----------------|----------------|----------------|------------------|----------------|
| | | E_{D} | E_{B} | E_{C} | E_{tot} | |
| (111) | O | -155 | 170 | -329 | -313 | 2787 |
| (100) | O | -239 | 448 | -366 | -157 | 2802 |
| (011) | O | -189 | 190 | -263 | -262 | 1785 |
| (121) | O | -161 | 225 | -540 | -476 | 2505 |
| (01 $\bar{1}$) | O | -308 | 409 | -487 | -387 | 2316 |
| (021) | O | -306 | 388 | -727 | -654 | 2703 |